RESEARCH ARTICLE
SOLID EARTH: EXPLORATION GEOPHYSICS

Earth and Planetary Physics
10: 75–81, 2026
doi: 10.26464/epp2026014

Redundant source-wavelet amplitude influence in wave-equation migration/demigration flow and its removal

QianCheng Liu[1,2*], JiaLe Kang[1,2], and Jie Li[1,2]

[1]State Key Laboratory of Lithospheric Evolution and Climate Change, Institute of Geology and Geophysics, Chinese Academy of Sciences, Beijing 100029, China;

[2]The College of Earth and Planetary Sciences, University of Chinese Academy of Sciences, Beijing 100049, China

Key Points:

- Redundant source wavelet distorts amplitudes and limits resolution in the wave-equation migration/demigration flow.
- We propose a source-equalized operator to remove redundancy and balances amplitudes.
- Numerical tests show reduced sidelobes, sharper reflectors, and improved consistency.

Citation: Liu, Q. C., Kang, J. L., and Li, J. (2026). Redundant source-wavelet amplitude influence in wave-equation migration/demigration flow and its removal. *Earth Planet. Phys.*, *10*(1), 75–81. http://doi.org/10.26464/epp2026014

Abstract: In wave-equation migration and demigration, the cross-correlation imaging/forwarding step implicitly injects an additional copy of the source wavelet, so that the amplitude spectrum of the wavelet is applied redundantly (effectively imposing a wavelet-spectrum weighting, often akin to an amplitude-squared bias). This redundancy degrades structural fidelity and amplitude balance yet is frequently overlooked. We (i) formalize the mechanism by which cross-correlation duplicates the source-wavelet amplitude effect in both migration and demigration, and (ii) introduce a source-equalized operator that removes the redundancy by deconvolving (or dividing by) the wavelet amplitude spectrum in the imaging condition and its demigration counterpart, while leaving phase/kinematics intact. Using a band-limited Ricker wavelet on a two-layer model and on Marmousi, we show that, if unmanaged, the redundant wavelet spectrum broadens main lobes, introduces ringing, and suppresses vertical resolution in migrated images, and inflates spectrum mismatches between demigrated and observed data even when peak times agree. With our correction, images recover observed-data-consistent bandwidth and sharpened interfaces, and demigrated data also exhibit improved spectrum conformity and reduced amplitude misfit. The results clarify when source amplitudes matter, why cross-correlation makes them redundantly matter, and how a lightweight spectral correction restores physically meaningful amplitude behavior in wave-equation migration/demigration.

Keywords: wave-equation migration; demigration; cross-correlation imaging condition; source wavelet; amplitude spectrum; spectral deconvolution

1. Introduction

Full wave-equation seismic migration, hereafter reverse-time migration (RTM; Whitmore, 1983), is central to high-resolution imaging of complex subsurface structure. By extrapolating recorded wavefields in the true physics, RTM exploits waveform kinematics and amplitudes to position reflectors with improved fidelity (Tarantola, 1987). The complementary full wave-equation demigration maps images back to the data domain to generate synthetic seismograms, providing a stringent consistency check on migration results (Santos et al., 2000; Dai W and Schuster, 2013). Together, they form a wave-equation migration/demigration flow, which is useful in seismic velocity and reflectivity inversion applications. In both procedures, accurate characterization of the source wavelet, the initial excitation that drives propagation (Virieux, 1986), is critical.

An ideal, albeit unattainable, source wavelet is an impulse with a flat amplitude spectrum across frequencies (Mendel, 2013). In practice, source wavelets are band-limited and taper-shaped; their amplitude spectra rarely meet this ideal. Field data commonly exhibit amplitude distortions (suppressed low/high-frequency lobes, erratic spectral ripples, and peak-frequency shifts) that (i) blur migrated images and bias amplitudes, and (ii) degrade consistency between demigrated and observed seismograms even when arrival phases align, thereby undermining waveform-based inversion and related analyses (Virieux and Operto, 2009). A broad literature has advanced migration and demigration in diverse settings: matched-filter RTM for monostatic/bistatic configurations (Leuschen and Plumb, 2001); time-reversal and minimum-variance strategies for target detection in uncertain media (Liu H et al., 2007); matrix-based LSRTM via generalized diffraction stacks (Yao G and Jakubowicz, 2016); 3D–to–2D data conversion enabling 2D RTM on 3D GPR acquisitions (Liu H et al., 2017); and fast, Wiener-filter-based LSRTM with extensions to

Correspondence to: Q. C. Liu, qliu@mail.iggcas.ac.cn
Received 07 AUG 2025; Accepted 15 OCT 2025.
First Published online 14 NOV 2025.

beam considerations, Gabor deconvolution for subsalt imaging, time-lapse, and true-amplitude imaging (Pratt, 1999; Liu QC and Peter, 2018; Liu QC et al., 2020a, b, 2024a, b). RTM has also been used to detect deep mantle discontinuities (Zhang ZD et al., 2023), and angle-related imaging conditions have improved steep-dip recoveries in acoustic/elastic RTM (Wang PF et al., 2024). Despite these progresses, how the source-wavelet amplitude spectrum systematically modulates wave-equation migration and demigration remains under-specified, particularly the fact that the standard cross-correlation step applies the wavelet's amplitude spectrum redundantly. This redundancy, which has been noticed by Liu QC et al. (2016) but not systematically in the wave-equation migration/demigration flow and in a unified framework, can overweight or underweight frequency bands twice, impairing resolution in migration and spectral conformity in demigration. Here we (i) diagnose the mechanism by which cross-correlation introduces a duplicate wavelet-amplitude effect, and (ii) present a lightweight source-equalized migration/demigration operator that removes this redundancy while preserving kinematics.

We organize this paper as follows. We first review the theoretical foundations of wave-equation migration and demigration. We then analyze how the band-limited source-wavelet amplitude spectrum influences these processes and derive a correction to remove the cross-correlation-induced redundancy. Next, we validate the approach with numerical experiments, and we conclude with key insights and practical guidance.

2. Theoretical Background

2.1 Fundamentals of Wave-Equation–Based Seismic Migration and Demigration

We consider the constant-density acoustic wave equation in the time domain,

$$\left(\frac{1}{v^2(\boldsymbol{x})}\frac{\partial^2}{\partial t^2}-\nabla^2\right)p(\boldsymbol{x},t;\boldsymbol{x}_S)=s(t;\boldsymbol{x}_S), \tag{1}$$

where $v(\boldsymbol{x})$ is the true velocity, p the pressure wavefield radiated by a source s located at $\boldsymbol{x}_S$. Let $v(\boldsymbol{x}) = v_0(\boldsymbol{x}) + \delta v(\boldsymbol{x})$ and linearize in δv to obtain the background/perturbation system

$$\begin{cases}\left(\dfrac{1}{v_0^2(\boldsymbol{x})}\dfrac{\partial^2}{\partial t^2}-\nabla^2\right)p_0(\boldsymbol{x},t;\boldsymbol{x}_S)=s(t;\boldsymbol{x}_S),\\[2ex] \left(\dfrac{1}{v_0^2(\boldsymbol{x})}\dfrac{\partial^2}{\partial t^2}-\nabla^2\right)\delta p(\boldsymbol{x},t;\boldsymbol{x}_S)=\dfrac{m(\boldsymbol{x})}{v_0^2(\boldsymbol{x})}\dfrac{\partial^2 p_0(\boldsymbol{x},t;\boldsymbol{x}_S)}{\partial t^2},\end{cases} \tag{2}$$

with logarithmic reflectivity $m(\boldsymbol{x}) = 2\,\delta v(\boldsymbol{x})/v_0(\boldsymbol{x})$ (Tromp et al., 2005; Dai W and Schuster, 2013). We use the Fourier convention $F(\omega) = \int f(t)\,\mathrm{e}^{-\mathrm{i}\omega t}\,\mathrm{d}t$ and write the source as $S(\omega) = W_S(\omega)$.

2.2 Migration (RTM)

Full wave-equation migration (RTM; Whitmore, 1983) back-propagates recorded data and applies a cross-correlation imaging condition (Tarantola, 1987). In the single-scattering (Born) setting,

$$D_R(\boldsymbol{x}_R,\omega;\boldsymbol{x}_S)=G_R(\boldsymbol{x}_R,\omega;\boldsymbol{x})\,m(\boldsymbol{x})\,G_S(\boldsymbol{x},\omega;\boldsymbol{x}_S)\,W_S(\omega), \tag{3}$$

where G_S, G_R are source/receiver Green's functions (*For brevity we suppress integrals over $\boldsymbol{x}$ when writing kernel forms). A standard cross-correlation imaging condition yields

$$I(\boldsymbol{x})=\iiint G_S(\boldsymbol{x},\omega;\boldsymbol{x}_S)\,W_S(\omega)\left[G_R(\boldsymbol{x},\omega;\boldsymbol{x}_R)\,D_R(\boldsymbol{x}_R,\omega;\boldsymbol{x}_S)\right]^*\mathrm{d}\omega\,\mathrm{d}\boldsymbol{x}_R\,\mathrm{d}\boldsymbol{x}_S. \tag{4}$$

Substituting Equation (3) gives an *implicit spectral weighting*

$$I(\boldsymbol{x})\propto\int|W_S(\omega)|^2\,\mathcal{K}(\boldsymbol{x},\omega)\,\mathrm{d}\omega, \tag{5}$$

i.e., the wavelet amplitude spectrum is applied *twice* (once in the data, once in the imaging condition). This cross-correlation-induced redundancy can blur interfaces and bias amplitudes, as illustrated in Figure 1.

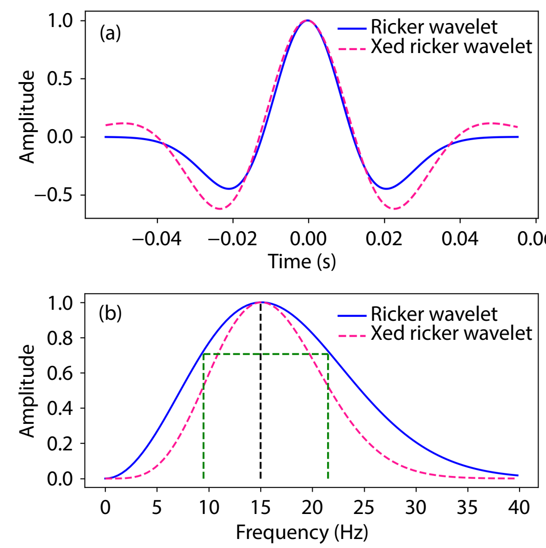

Figure 1. Comparison between the original Ricker wavelet and its cross-correlated (autocorrelated, Xed for short) counterpart in the (a) time and (b) frequency domains. The plots have been normalized. The cross-correlation imaging condition imposes a redundant spectral weighting, effectively squaring the wavelet's amplitude spectrum to $|W_S(\omega)|^2$. In (a), the dashed trace shows enhanced sidelobes/ripples that degrade imaging resolution; in (b), the dashed curve exhibits a narrower effective bandwidth, implying loss of high- and low-frequency content. The black dashed line marks the peak frequency and green lines indicate the 3-dB bandwidth.

2.3 Demigration (Forward to Data)

Wave-equation demigration maps an image $m(\boldsymbol{x})$ to synthetic data by forward propagation with the same physics (Dai W and Schuster, 2013). Using Equations (2) and (3), the demigrated data read

$$D_{\text{demig}}(\boldsymbol{x}_R,\omega;\boldsymbol{x}_S)=G_R(\boldsymbol{x}_R,\omega;\boldsymbol{x})\,I(\boldsymbol{x})\,G_S(\boldsymbol{x},\omega;\boldsymbol{x}_S)\,W_S(\omega), \tag{6}$$

so that the same $|W_S(\omega)|$ factor enters again. If I was already formed under Equation (5), the aggregate effect in the data–model loop is a redundant amplitude weighting that degrades spectrum conformity.

2.4 Removing the Redundancy

To alleviate the redundant amplitude action of the source wavelet, we precondition the data (trace by trace) before imaging by a stabilized inverse spectrum:

$$\tilde{D}_R(\boldsymbol{x}_R,\omega;\boldsymbol{x}_S)=\frac{D_R(\boldsymbol{x}_R,\omega;\boldsymbol{x}_S)}{|W_S(\omega)|+\epsilon}, \tag{7}$$

with a small stabilizer ϵ and band-limited taper confined to $[\omega_{\min},\omega_{\max}]$. The imaging condition becomes

$$I(\boldsymbol{x})=\iiint G_S(\boldsymbol{x},\omega;\boldsymbol{x}_S)\,W_S(\omega)\left[G_R(\boldsymbol{x},\omega;\boldsymbol{x}_R)\,\tilde{D}_R(\boldsymbol{x}_R,\omega;\boldsymbol{x}_S)\right]^{*}\mathrm{d}\omega\,\mathrm{d}\boldsymbol{x}_R\,\mathrm{d}\boldsymbol{x}_S, \tag{8}$$

which cancels the extra $|W_S|$ and restores reflectivity-consistent bandwidth while preserving phase/kinematics. Analogously, for demigration we apply

$$\tilde{D}_{\mathrm{demig}}(\boldsymbol{x}_R,\omega;\boldsymbol{x}_S)=\frac{D_{\mathrm{demig}}(\boldsymbol{x}_R,\omega;\boldsymbol{x}_S)}{|W_S(\omega)|+\epsilon} \tag{9}$$

to remove the redundant amplitude factor in the data domain. In practice, $|W_S(\omega)|$ is estimated from near-offset direct arrivals or multitrace robust spectral averages after instrument-response removal. The stabilized division is applied only within a trusted band $[\omega_{\min},\omega_{\max}]$ with a cosine (or Tukey) taper, and ϵ is set to 1%–5% of the spectral peak to suppress noise amplification.

2.5 On Amplitude Content in Band-Limited Source Wavelets

A practical source wavelet is band-limited with $\omega\in[\omega_{\min},\omega_{\max}]$ and tapered near band edges (Ricker, 1953; Wang YH et al., 2015). Under the cross-correlation imaging condition (Etgen et al. 2009), such wavelets act as tapered band-pass filters, imposing $|W_S(\omega)|^2$ on the imaged spectrum, which broadens mainlobes and introduces sidelobes/ringing in time (Figure 1a).

Amplitude fidelity, which is critical for reservoir characterization, can be compromised when spectral shapes are unfavorable (e.g., skewed rather than symmetric $|W_S(\omega)|$), biasing amplitude estimates (Wang YH et al., 2015); rippled $|W_S(\omega)|$ can imprint spurious spatial variations that mimic attenuation anomalies (Savage et al., 2010). In demigration, the synthetic data further inherit the additional $|W_S(\omega)|$ factor, degrading spectrum conformity to observations even when arrival phases match. These considerations motivate removing the redundant wavelet-amplitude effect in both migration and demigration.

2.6 Practical Field Considerations

Field shot gathers often contain multiple interfering effects (random noise, residual statics, surface-wave contamination, inter-shot crosstalk, and velocity-model imperfections). Our correction does not attempt to remove these phenomena; it solely prevents *redundant* spectral weighting of the data by the source wavelet. Importantly, RTM kinematics are governed primarily by the propagation operator and the background velocity, so a *rough* but smoothed estimate of $|W_S(\omega)|$ is typically sufficient to realize most of the benefit: removing one extra copy of the amplitude spectrum. Any residual error in $|W_S(\omega)|$ manifests mainly as a mild amplitude tilt rather than a loss of structural positioning. In practice, we (i) estimate a band-limited, smoothly tapered envelope of $|W_S(\omega)|$, (ii) apply stabilized division only within the trusted band, and (iii) avoid equalization where the signal-to-noise ratio is poor. This keeps the procedure robust on field data while leaving the underlying kinematics intact, although we do not involve field-data practices in this paper.

3. NumericaL Examples

3.1 Two-Layer Model

We first verify the methodology on a simple two-layer model (Figure 2a) with velocities of 2000 m/s and 2500 m/s. Wavefield simulations use a staggered-grid finite-difference scheme (Virieux, 1986) with a 15 Hz Ricker source-time function. Figures 2b and 2c show RTM images produced by the conventional cross-correlation imaging condition and by our source-wavelet-equalized imaging condition, respectively. Exaggerated traces (highlighted in deep pink) indicate that the equalized image exhibits a sharper interface and reduced sidelobes, reflecting improved vertical resolution.

We next examine demigration. Figures 2d–2f display the observed data, the demigrated data using the conventional workflow, and the demigrated data after removing the redundant source-wavelet amplitude factor. The conventional demigrated gathers show prominent sidelobes and ripples, whereas the equalized demigrated data more closely resemble the observations. These qualitative gains will be quantified on the Marmousi model below.

3.2 Marmousi Model

We then test the approach on the Marmousi model (Versteeg, 1994), which features strong lateral and vertical heterogeneity. The true model and the background migration model are shown in Figures 3a and 3b. Simulations again use a staggered-grid scheme (Virieux, 1986) with perfectly matched layers (PML) (Komatitsch and Martin, 2007). Thirty shots are fired near the surface; receivers are deployed along the surface.

Figures 4a and 4b compare RTM images obtained with the conventional and source-wavelet equalized imaging conditions. A visual inspection suggests that Figure 4b preserves crisper reflectors and attenuates ringing relative to Figure 4a. To quantify the impact, we adopt the normalized cross-correlation (NCC) between the reflectivity reference and the image, evaluated depth-wise. Figure 4d shows that the equalized image achieves systematically higher NCC across most depths. While the gain is moderate, as expected for illumination-limited imaging (Guitton et al., 2007), it is nevertheless consistent and meaningful. The NCC decreases toward the lateral ends because of poorer acquisition coverage there.

For demigration, we start from the equalized image (Figure 4b). Figure 5a shows the observed data; Figures 5b and 5c show demigrated data from the conventional and equalized workflows, respectively. Signals in Figure 5c are notably cleaner and less rippled than in Figure 5b. The NCC between the observed and demigrated data (trace-wise) is plotted in Figure 5d, demonstrating a clear shift toward unity after source-wavelet equalization. This improvement is achieved with minimal additional cost via stabilized division by $|W_S(\omega)|$ in the trusted band.

4. Discussion and Conclusion

This study investigated how the amplitude spectrum of a band-

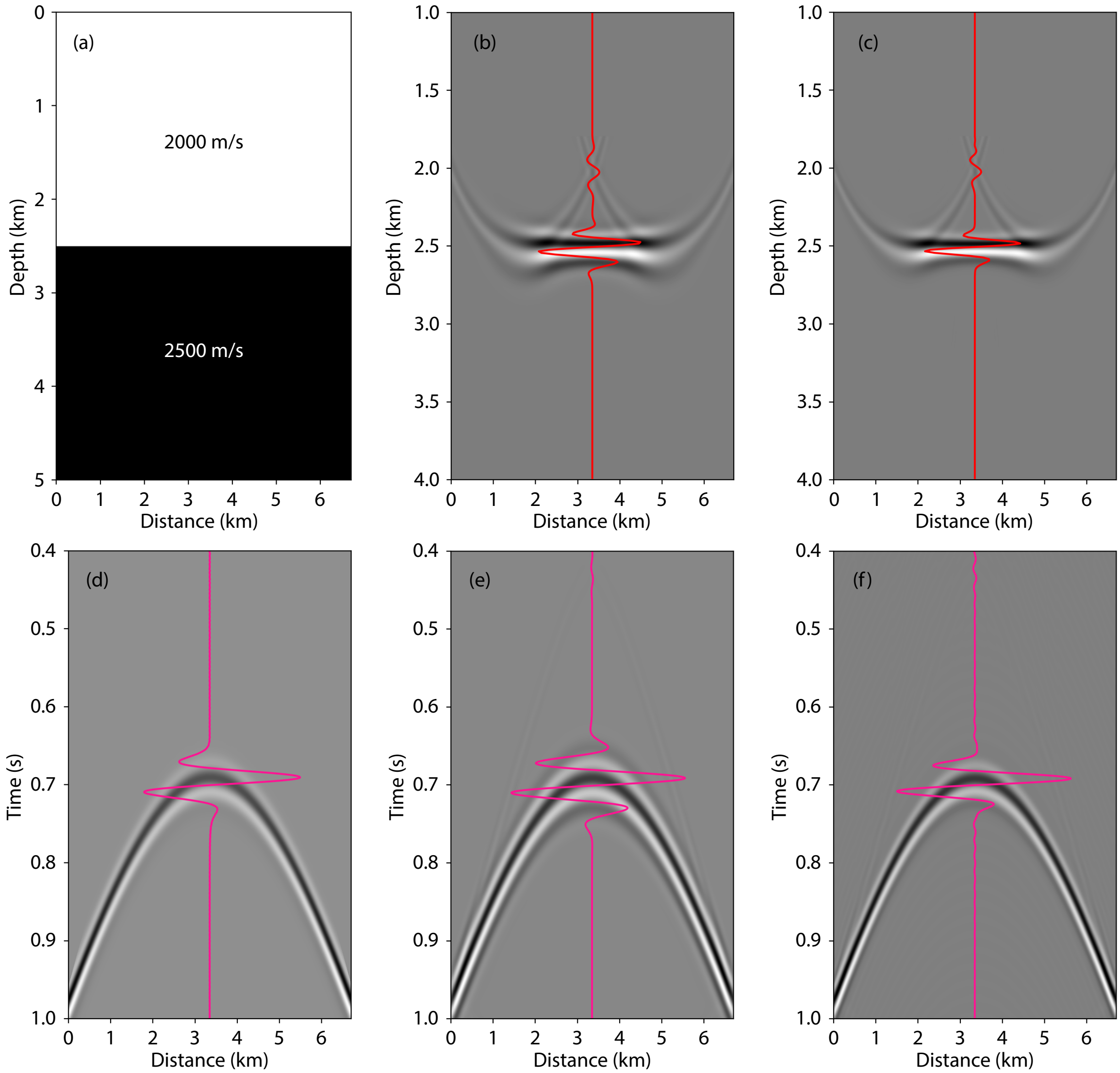

Figure 2. Two-layer example. (a) True model; (b) RTM image with the conventional cross-correlation imaging condition; (c) RTM image with the source-wavelet-equalized imaging condition; (d) observed data; (e) demigrated data from (c) without equalization; (f) demigrated data with source-wavelet equalization. Panel (c) exhibits a sharper interface and reduced sidelobes relative to (b), and panel (f) shows higher resemblance to the observations in (d). The improvements result from removing the redundant source-wavelet amplitude effect.

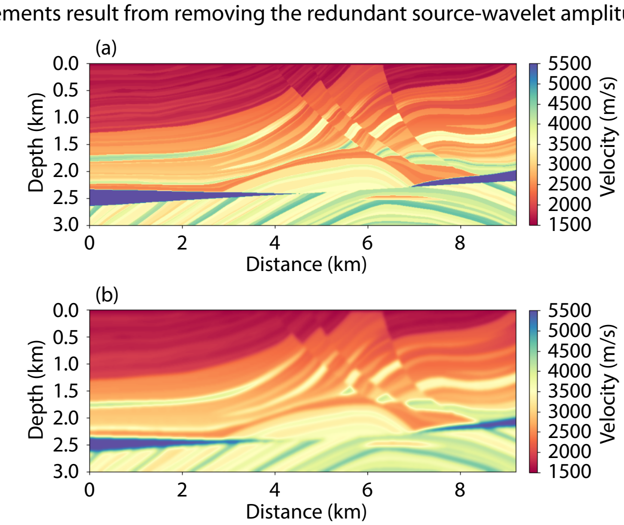

Figure 3. (a) True Marmousi model used to generate the observed data. (b) Background (smoothed) Marmousi model used for migration and demigration, obtained from (a) by suppressing high-wavenumber content.

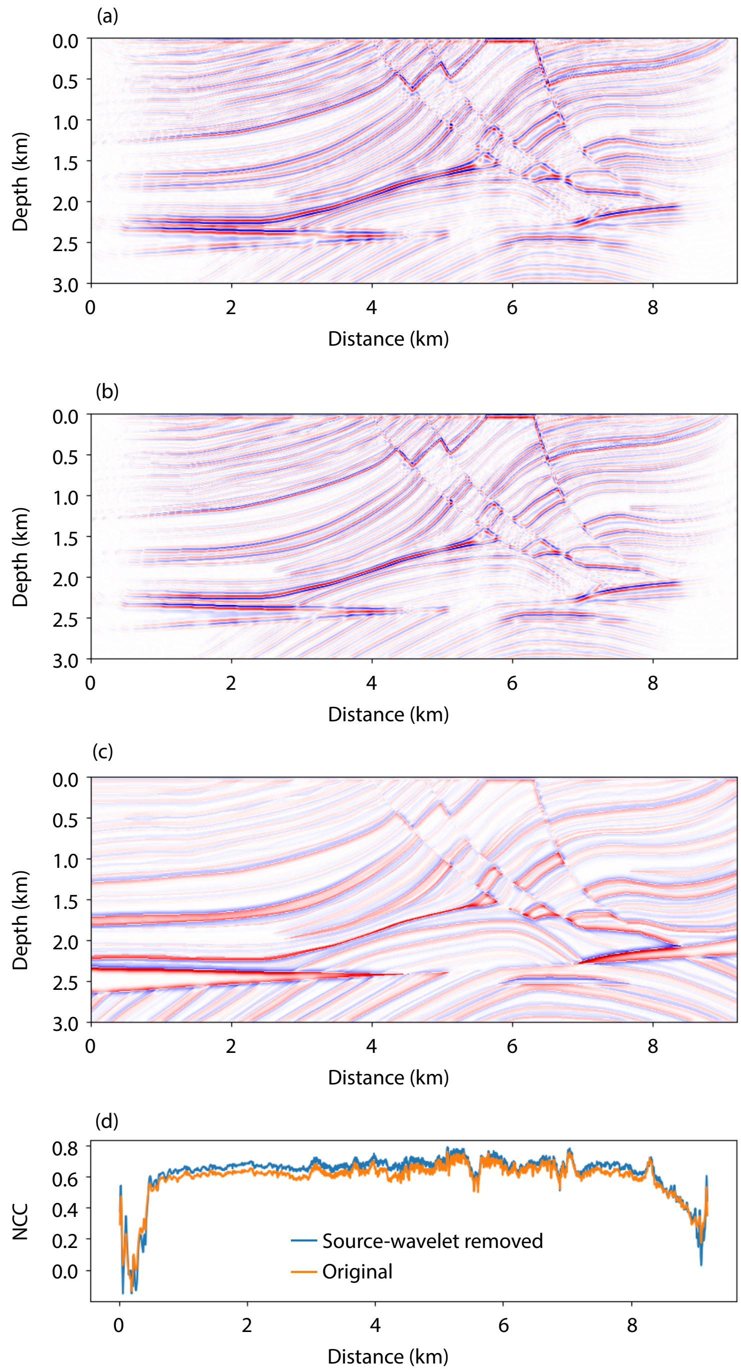

Figure 4. (a) Migration image (illumination-normalized) obtained with the conventional cross-correlation imaging condition; (b) migration image produced by the same workflow as in (a) but with additional source-wavelet equalization (removal of the redundant amplitude factor); (c) reference reflectivity model; (d) depth-wise normalized cross-correlation (NCC) between the images and the reference. Panel (b) more closely resembles (c) and exhibits notably higher resolution than (a). The NCC curves in (d) quantify this improvement, showing systematically higher similarity after source-wavelet removal.

limited source wavelet affects wave-equation migration and demigration, and how a lightweight correction removes the cross-correlation–induced redundancy. The key points are as follows. *Redundancy mechanism:* the conventional cross-correlation imaging/forwarding step applies the source-wavelet amplitude spectrum twice, yielding an implicit $|W_S(\omega)|^2$ weighting that broadens mainlobes, enhances sidelobes, and biases amplitudes. *Equalization strategy:* a stabilized, band-limited preconditioning of data (trace-by-trace) by $\left(|W_S(\omega)|+\epsilon\right)^{-1}$ prior to imaging, and the analogous operation in demigration, removes the redundant amplitude factor while preserving kinematics and phase. *Numerical evidence:* on a two-layer model and on Marmousi (with a Ricker wavelet), equalization sharpens interfaces, suppresses ringing, and improves spectrum conformity of demigrated data. Depth-wise and trace-wise NCC metrics confirm consistent gains. These results underscore that accounting for the band-limited wavelet

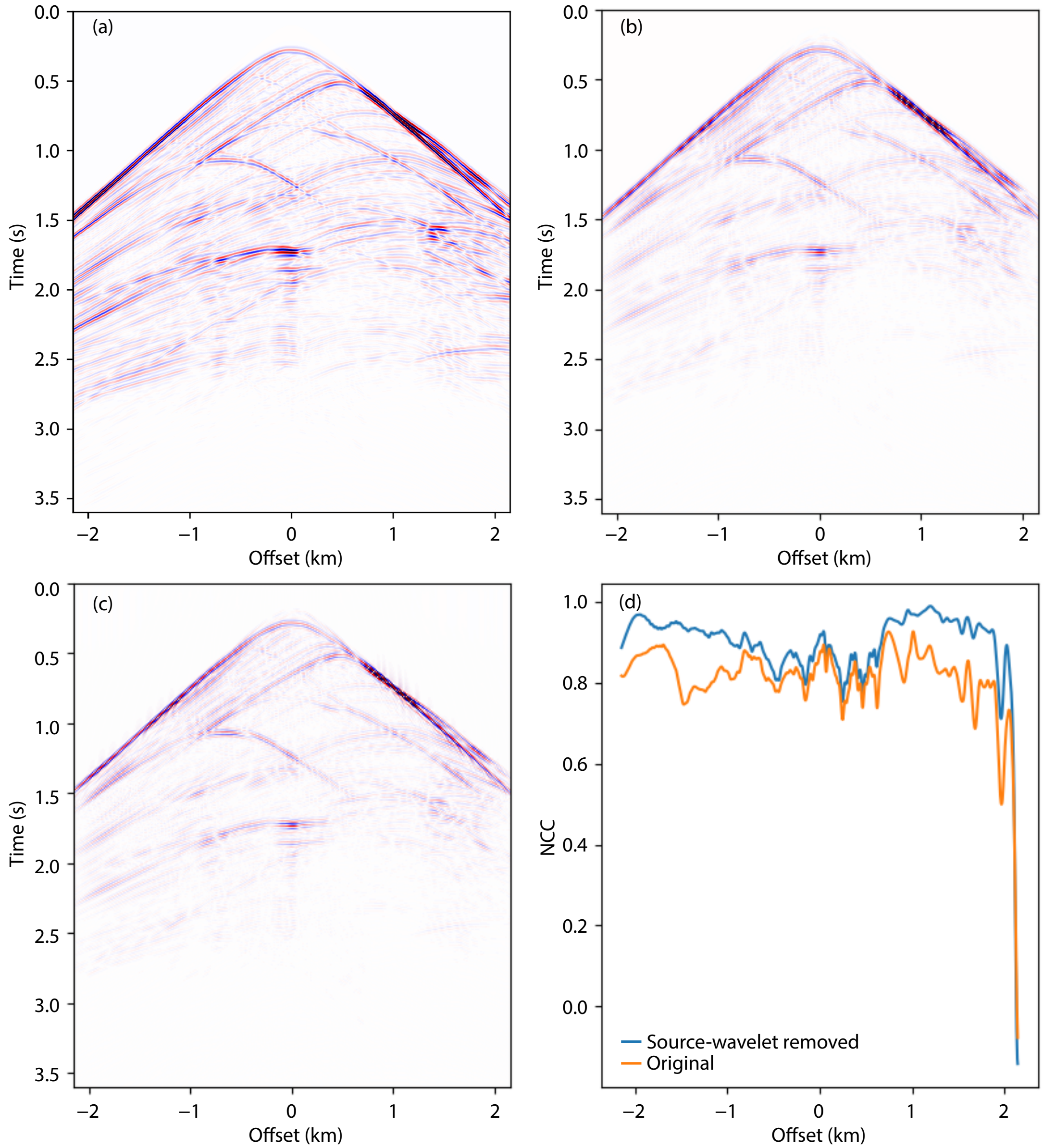

Figure 5. Common-shot gathers for a source at x = 5.15 km. (a) Observed data; (b) demigrated data without source-wavelet equalization; (c) demigrated data with source-wavelet equalization; (d) similarity to (a) quantified by trace-wise normalized cross-correlation (NCC) for (b) and (c). Removing the redundant source-wavelet amplitude factor yields visibly cleaner waveforms in (c) and a clear shift of the NCC curve toward unity in (d), indicating improved consistency between observed and demigrated datasets.

amplitude spectrum, and explicitly removing its redundant application, is important for both imaging fidelity and data-model consistency. Future work could integrate adaptive estimation of $|W_S(\omega)|$ (e.g., multitrace robust averaging, time-varying spectral shaping) and extend the equalization to angle-domain or least-squares migration frameworks.

Acknowledgments

The research in this publication was supported by the National Natural Science Foundation of China (42430303), Strategy Priority Research Program (Category B) of the Chinese Academy of Sciences (XDB0710000), National Natural Science Foundation of China (42288201), the National Key R&D Program of China (2023YFF0803203), and the IGGCAS start-up funding (Grant No. E251510101).

References

Dai, W., and Schuster, G. T. (2013). Plane-wave least-squares reverse-time migration. *Geophysics*, *78*(4), S165–S177. https://doi.org/10.1190/geo2012-0377.1

Etgen, J., Gray, S. H., and Zhang, Y. (2009). An overview of depth imaging in exploration geophysics. *Geophysics*, *74*(6), WCA5–WCA17. https://doi.org/10.1190/1.3223188

Guitton, A., Valenciano, A., Bevc, D., and Claerbout, J. (2007). Smoothing imaging condition for shot-profile migration. *Geophysics*, *72*(3), S149–S154. https://doi.org/10.1190/1.2712113

Komatitsch, D., and Martin, R. (2007). An unsplit convolutional perfectly matched layer improved at grazing incidence for the seismic wave equation. *Geophysics*, *72*, SM155–SM167. https://doi.org/10.1190/1.

2757586

Leuschen, C. J., and Plumb, R. G. (2001). A matched-filter-based reverse-time migration algorithm for ground-penetrating radar data. *IEEE Trans. Geosci. Remote Sens.*, *39*(5), 929–936. https://doi.org/10.1109/36.921410

Liu, D. H., Krolik, J., and Carin, L. (2007). Electromagnetic target detection in uncertain media: Time-reversal and minimum-variance algorithms. *IEEE Trans. Geosci. Remote Sens.*, *45*(4), 934–944. https://doi.org/10.1109/TGRS.2006.890411

Liu, H., Long, Z. J., Tian, B., Han, F., Fang, G. Y., and Liu, Q. H. (2017). Two-dimensional reverse-time migration applied to GPR with a 3-D-to-2-D data conversion. *IEEE J. Sel. Top. Appl. Earth Observations Remote Sens.*, *10*(10), 4313–4320. https://doi.org/10.1109/JSTARS.2017.2734098

Liu, Q. C., Zhang, J. F., and Zhang, H. (2016). Eliminating the redundant source effects from the cross-correlation reverse-time migration using a modified stablized division. *Comput. Geosci.*, *92*, 49–57. https://doi.org/10.1016/j.cageo.2016.04.001

Liu, Q. C., and Peter, D. (2018). One-step data-domain least-squares reverse time migration. *Geophysics*, *83*(4), R361–R368. https://doi.org/10.1190/geo2017-0622.1

Liu, Q. C., Lu, Y. M., Sun, H., and Zhang, H. (2020a). Single-step data-domain least-squares reverse-time migration using Gabor deconvolution for subsalt imaging. *IEEE Geosci. Remote Sens. Lett.*, *17*(1), 13–16. https://doi.org/10.1109/LGRS.2019.2916847

Liu, Q. C., Lu, Y. M., and Zhang, H. (2020b). Fast single-step least-squares reverse-time imaging via adaptive matching filters in beams. *IEEE Trans. Geosci. Remote Sens.*, *58*(3), 1913–1919. https://doi.org/10.1109/TGRS.2019.2950645

Liu, Q. C., Chen, L., and Xu, J. C. (2024a). Time-lapse one-step least-squares migration. *IEEE Geosci. Remote Sens. Lett.*, *21*, 3000404. https://doi.org/10.1109/LGRS.2023.3344695

Liu, Q. C., Chen, L., and Zhao, L. (2024b). Seismic true-amplitude imaging: A data-domain amplitude-matching perspective. *IEEE Geosci. Remote Sens. Lett.*, *21*, 3004204. https://doi.org/10.1109/LGRS.2024.3459635

Mendel, J. M. (2013). *Optimal seismic Deconvolution*: *An Estimation-Based Approach*. New York: Academic Press.

Pratt, R. G. (1999). Seismic waveform inversion in the frequency domain. Part 1: theory and verification in a physical scale model. *Geophysics*, *64*(3), 888–901.

Ricker, N. (1953). The form and laws of propagation of seismic wavelets. *Geophysics*, *18*(1), 10–40. https://doi.org/10.1190/1.1437843

Santos, L. T., Schleicher, J., Tygel, M., and Hubral, P. (2000). Seismic modeling by demigration. *Geophysics*, *65*(4), 1281–1289. https://doi.org/10.1190/1.1444819

Savage, B., Komatitsch, D., and Tromp, J. (2010). Effects of 3D attenuation on seismic wave amplitude and phase measurements. *Bull. Seismol. Soc. Am.*, *100*(3), 1241–1251. https://doi.org/10.1785/0120090263

Tarantola, A. (1987). *Inverse Problem Theory*: *Methods for Data Fitting and Model Parameter Estimation*. New York: Elsevier.

Tromp, J., Tape, C., and Liu, Q. Y. (2005). Seismic tomography, adjoint methods, time reversal and banana-doughnut kernels. *Geophys. J. Int.*, *160*(1), 195–216. https://doi.org/10.1111/j.1365-246X.2004.02453.x

Versteeg, R. (1994). The Marmousi experience: Velocity model determination on a synthetic complex data set. *The Leading Edge*, *13*(9), pp. 927–936.

Virieux, J. (1986). *P-SV* wave propagation in heterogeneous media: velocity-stress finite-difference method. *Geophysics*, *51*(4), 889–901. https://doi.org/10.1190/1.1442147

Virieux, J., and Operto, S. (2009). An overview of full-waveform inversion in exploration geophysics. *Geophysics*, *74*(6), WCC1–WCC26. https://doi.org/10.1190/1.3238367

Wang, P. F., Yang, J. D., Huang, J. P., Sun, J. X., and Tian, Y. W. (2024). Acoustic and elastic reverse-time migration with an angle-related imaging condition for imaging steeply-dipping structures. *IEEE Trans. Geosci. Remote Sens.*, *62*, 5927308. https://doi.org/10.1109/TGRS.2024.3458148

Wang, Y. H. (2015). Generalized seismic wavelets. *Geophys. J. Int.*, *203*(2), 1172–1178. https://doi.org/10.1093/gji/ggv346

Whitmore, N. D. (1983). Iterative depth migration by backward time propagation. In *Proceedings of the SEG Technical Program Expanded Abstracts 1983* (pp. 382–385). SEG. https://doi.org/10.1190/1.1893867

Yao, G., and Jakubowicz, H. (2016). Least-squares reverse-time migration in a matrix-based formulation. *Geophys. Prospect.*, *64*(3), 611–621. https://doi.org/10.1111/1365-2478.12305

Zhang, Z. D., Irving, J. C. E., Simons, F. J., and Alkhalifah, T. (2023). Seismic evidence for a 1000 km mantle discontinuity under the pacific. *Nat. Commun.*, *14*(1), 1714. https://doi.org/10.1038/s41467-023-37067-x